


# Arduino-based slider setup for gas–liquid mass transfer investigations: Experiments and CFD simulations

Waldemar Krieger<sup>1</sup>  | Evren Bayraktar<sup>2</sup> | Otto Mierka<sup>2</sup> | Lutz Kaiser<sup>1</sup> | Robin Dinter<sup>1</sup> | Julian Hennekes<sup>1</sup> | Stefan Turek<sup>2</sup> | Norbert Kockmann<sup>1</sup>

<sup>1</sup>Department of Biochemical and Chemical Engineering, Laboratory of Equipment Design, TU Dortmund University, Dortmund, Germany

<sup>2</sup>Department of Mathematics, Institute of Applied Mathematics, TU Dortmund University, Dortmund, Germany

## Correspondence

Waldemar Krieger, Department of Biochemical and Chemical Engineering, Laboratory of Equipment Design, TU Dortmund University, Emil-Figge-Strasse 68, Dortmund 44227, Germany.

Email: waldemar.krieger@tu-dortmund.de

Evren Bayraktar, Department of Mathematics, Institute of Applied Mathematics: Chair III, TU Dortmund University, Vogelpothsweg 87, Dortmund 44227, Germany.

Email: evren.bayraktar@tu-dortmund.de

## Funding information

Deutsche Forschungsgemeinschaft, Grant/Award Numbers: KO2349/13-1, TU 102/53-1

## Abstract

The implementation of traditional sensors is a drawback when investigating mass transfer phenomena within microstructured devices, since they disturb the flow and reactor characteristics. An Arduino based slider setup is developed, which is equipped with a computer-vision system to track gas–liquid slug flow. This setup is combined with an optical analytical method allowing to compare experimental results against CFD simulations and investigate the entire lifetime of a single liquid slug with high spatial and temporal resolution. Volumetric mass transfer coefficients are measured and compared with data from literature and the mass transfer contribution of the liquid film is discussed.

## KEYWORDS

Arduino based microcontroller, gas–liquid capillary flow, local mass transfer, noninvasive measurement, numerical simulation

## 1 | INTRODUCTION

Recently, flow chemistry in microreactors has become an alternative to conventional batch processes.<sup>1,2</sup> Enhanced heat and mass transfer due to high surface-to-volume ratios make microstructured devices a promising technology to overcome mass transfer limitations for example, in gas–liquid reactions.<sup>3</sup> When investigating mass transfer phenomena within microstructured devices, the implementation of traditional sensors and analytical methods is a drawback, since they disturb the flow and reactor characteristics. In order to study gas–liquid mass transfer, offline and online measurement techniques are commonly used besides numerical approaches. Offline measurement techniques provide limited insight into flow structure and usually consider only two points of the microchannel (inlet and outlet)<sup>4,5</sup> while noninvasive online measurement techniques either cannot provide

local results (optical measurement of bubble shrinkage)<sup>6</sup> or require a sophisticated setup such as laser-induced fluorescence, to resolve concentration profiles of the dissolved gas.<sup>7,8</sup> Dietrich et al.<sup>9</sup> proposed a colorimetric approach utilizing the oxidation of dihydroresorufin and its color change from colorless to pink for the measurement of absorbed oxygen. They developed an image processing method to convert grayscale images into concentration distributions of oxidized product resorufin. Kováts et al.<sup>10</sup> performed similar studies in coiled capillaries with methylene blue as redox dye. Krieger et al.<sup>11</sup> extended this method to color images with the consecutive oxidation of leuco-indigo carmine (LIC), which exhibits two distinct color changes (yellow–red–blue), allowing for conclusions regarding selectivity of chemical gas–liquid reactions. Computational fluid dynamics (CFDs) simulations are employed to support the experimental observations in order to present a more complete picture of microflows.<sup>12</sup> The perhaps

This is an open access article under the terms of the Creative Commons Attribution License, which permits use, distribution and reproduction in any medium, provided the original work is properly cited.

© 2020 The Authors. *AIChE Journal* published by Wiley Periodicals, Inc. on behalf of American Institute of Chemical Engineers.

most comprehensive study on the numerical simulation of slug flows in capillaries was performed from Falconi et al.<sup>13</sup> They extend an open-source flow solver with Continuous-Species-Transform Method in free-surface flows and study in detail Taylor flow in a rectangular channel. Main message of this brief review is that at the state of art the researchers are still in need of a comprehensive CFD flow solver, which can tackle the challenges of reacting slug flows in capillaries.

Another trend in micro process engineering is the integration of low-cost automation based on open-source technology in order to improve laboratory safety and reduce time-consuming practices.<sup>14</sup> Computer-vision controlled liquid-liquid extraction steps are reported in literature that facilitate the automation of an iodination and desilylation reaction by utilizing a Raspberry Pi single-board computer and open-source software technologies such as Python and OpenCV.<sup>15,16</sup> A liquid-handling chemorobotic platform based on the open-source “RepRap” 3D printer with OpenCV as core component for the computer-vision system was used by Gutierrez et al. to investigate the properties of oil droplets via an automated evolutionary process.<sup>17</sup> Taking advantage of such technologies is a key step to improve equipment usage and availability, increase research efficiency in future,<sup>14</sup> prototype self-regulating, and adaptive chemical equipment and explore complex chemical systems.<sup>17,18</sup>

In this work, an Arduino based slider setup is developed, which is equipped with a computer-vision system to track single slugs of gas-liquid slug flow. This setup is combined with an optical analytical method utilizing the oxidation of leuco-indigo carmine in order to study flow structure, selectivity and mass transfer phenomena in gas-liquid slug flow with high temporal and spatial resolution. Furthermore, differences between slug flow with and without a liquid film surrounding the gas bubbles are analyzed and discussed. The experimental work is complemented with numerical simulations, that are performed with FeatFlow (<https://www.featflow.de>), which is a multi-purpose CFD software package developed by Turek et al. FeatFlow uses a higher order finite element method (FEM,  $Q_2$ ) to treat generalized unstructured hexahedral meshes. FeatFlow is a well-established open-source flow solver capable of solving challenging benchmark problems.<sup>19,20</sup> For this work, in order to simulate reactive slug flow, FeatFlow is extended with (a) surface tracking method within an arbitrary Lagrangian-Eulerian (ALE) approach, (b) moving reference frame, and (c) an ode-solver for consecutive chemical reactions. By combining a slug flow tracking setup with an analytical method that provides local mass transfer information, the entire lifetime of a single slug is captured providing valuable data for the development of theoretical models and validation of the numerical simulations.

## 2 | MATERIALS AND METHODS

### 2.1 | Oxidation of leuco-indigo carmine

The use of redox dyes for the visualization of gas-liquid mass transfer in optical accessible capillaries or microchannels is a promising approach for the investigation of gas-liquid mass transfer with high

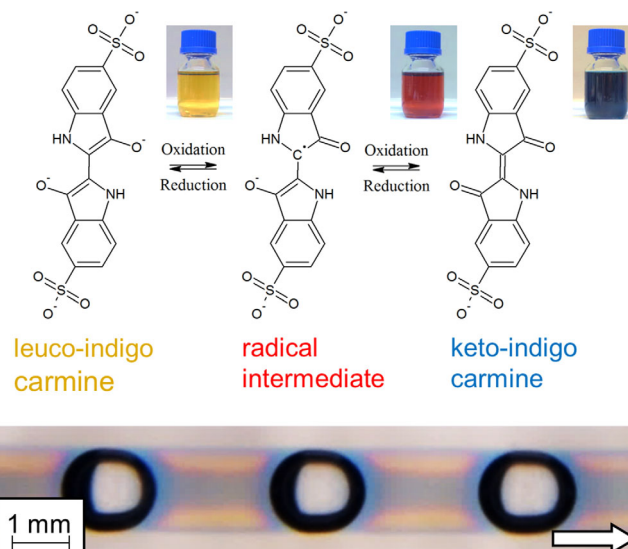
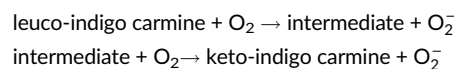


**FIGURE 1** Redox reaction of leuco-indigo carmine to keto-indigo carmine in flask experiments and in capillary flow. Adapted from Sousa et al.<sup>21</sup> [Color figure can be viewed at [wileyonlinelibrary.com](http://wileyonlinelibrary.com)]

spatial and temporal resolution. For this work, the oxidation of leuco-indigo carmine over an intermediate form (Int) to keto-indigo carmine (KIC) is utilized since it undergoes two color changes from yellow to red to blue (Figure 1), which provides additional information regarding the selectivity of fast consecutive gas-liquid reactions. The reaction equations for the oxidation steps are as follows:



This reaction can be reversed by introducing glucose in alkaline solution.<sup>11</sup>

Since two color changes occur, the image processing routine has been extended to color images in a previous work.<sup>11</sup> The relevant processing steps are as follows:

- Subtraction of background image
- Masking of gas bubbles
- Extraction of color channels (CMY)
- Color compensation due to varying liquid phase thickness
- Conversion of color intensity to concentration

The calibration and validation were performed by means of UV spectroscopy.<sup>11</sup>

## 2.2 | Slug flow tracking system

### 2.2.1 | Slider design

A slider system is developed which carries a DSLR camera (Nikon DS 5300) for mass transfer analysis and uses a Pixy CMUcam5 as vision sensor board for object detection. The vision sensor transfers images at a frequency of 50 Hz and a resolution of 1,280 × 800 with

an on-board image processing algorithm which enables the detection of colored objects. Pixy and slider communicate via a microcontroller, Arduino Uno. The Arduino Uno is connected through a driver (DRV8825, Pololu, USA) to a stepper motor (NEMA17, Trinamic Motion Control, Germany) which moves the slider. The electrical circuit diagram is shown in Figure 2, for which the wiring is done on an Arduino shield by soldering every connection. Note that an additional 12 V power supply and a capacitor are included to provide the necessary voltage for the stepper motor and protect the driver from voltage peaks. Limit switches are incorporated in order to stop the slider at the edges of the guide rail independent from the vision sensor.

The setup is constructed with a PID controller to enable flow tracking; nevertheless, the vision sensor board could neither precisely capture slug nor bubble position, which resulted in inaccurate tracking behavior. Therefore, a potentiometer is used to manually track the flow by observing live images from the graphical user interface (GUI) PixyMon. Additionally, an initial stepper motor speed is set to match the expected flow velocity and reduce the number of required control interventions.

The mechanical parts for the slider setup include a guide rail with support feet and a guide carriage (IGUS, Germany). The construction containing DSLR camera, Pixy cam and LED panels (Kaiser Fototechnik, Germany) are made in-house and attached to the guide carriage. Guide carriage and stepper motor are connected via a toothed belt (BIQU, China). The complete setup combined with the microfluidic setup is shown in Figure 3. The effective tube length that can be captured by the DSRL camera is 500 mm long.

## 2.2.2 | Microfluidic setup

Capillaries, which are used as gas–liquid reactors, are fabricated from FEP (fluorinated ethylene propylene) tubes with inner diameter of 1.6 mm. Total volumetric flow rate is varied in the range of

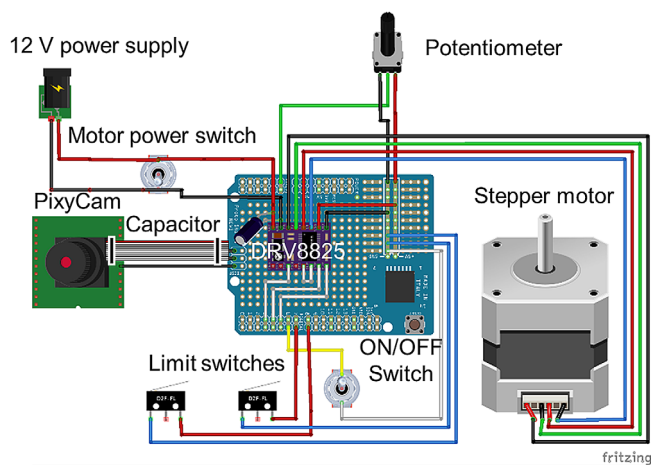


**FIGURE 2** Circuit diagram for Arduino board with stepper motor incl. Driver, Pixy, potentiometer, power supply and limit switches. Created with open source software fritzing [Color figure can be viewed at [wileyonlinelibrary.com](#)]

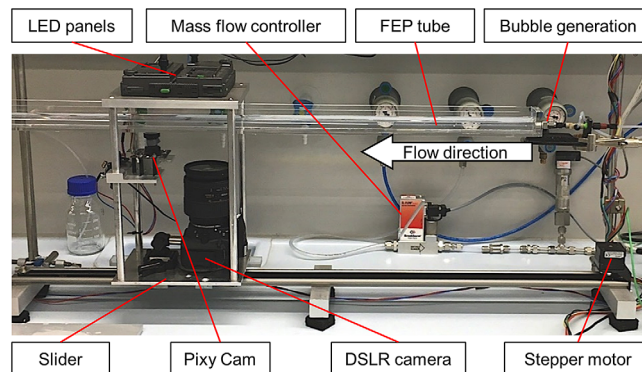


**FIGURE 3** Experimental setup for developed slug flow tracking system including setup for gas–liquid slug flow generation [Color figure can be viewed at [wileyonlinelibrary.com](#)]

4.0–10.0 ml min<sup>-1</sup> and volumetric flow ratios (gas/liquid ratio) in the range of 0.33–1.0 ( $= \dot{V}_G/\dot{V}_L$ ). Liquid phase is pumped continuously by a piston pump (Knauer, Germany) and synthetic air flow rate is regulated by a mass flow controller (Bronkhorst, the Netherlands). A pressure sensor and a type K thermocouple are used to measure pressure and temperature in the gas inlet. Slug flow is generated with a hypodermic needle, which is placed in the center of the FEP tube's inlet within a T-junction. FEP capillary is positioned horizontally inside a PMMA box filled with deionized water in order to reduce light refraction ( $n_{\text{Water}} = 1.333$ ,  $n_{\text{FEP}} = 1.338$ ).<sup>22</sup>

## 2.3 | Mass transfer investigation

Keto-indigo carmine (0.2 g L<sup>-1</sup>) is reduced to leuco-indigo carmine by glucose (54 g L<sup>-1</sup>) in alkaline solution (4 g L<sup>-1</sup> NaOH) while being degassed with nitrogen to prevent reoxidation by ambient air. This solution acts as liquid phase to generate slug flow as described in Section 2.2.2. A start-up routine is used to influence the occurrence of a liquid film surrounding the gas phase. Slug flow without a liquid film will be referred to as dry slug flow and slug flow with liquid film as film slug flow. Experiments are initiated with low gas and liquid flowrates, then both flow rates are gradually increased until the desired flow condition is reached so that dry slug flow is generated. In order to generate film slug flow, high gas and liquid flow rates are set at the beginning. Later, the gas flow rate is decreased and liquid flow rate increased until the desired conditions are reached. Besides, polysorbate 80 is added as surfactant (0.005–0.1% v/v) to assist film formation in a separate set of experiments. Its influence on mass transfer is discussed in Section 4.2.1.

During mass transfer investigations with the designed slider videos of the reactive slug flow are recorded with 50 frames per second. The developed image processing routine (Section 2.1) requires background and compensation images to reduce effects of inhomogeneous illumination and deal with the varying liquid phase thickness of circular tubes. More details can be found in Krieger et al.<sup>11</sup> In order to transfer the image processing routine to videos, the time of a video

capturing the gas–liquid reaction is measured and used to record background and compensation videos with the same number of frames. For the background video the FEP capillary is filled with deionized water and for the compensation video it is filled with  $0.2 \text{ g L}^{-1}$  keto-indigo carmine solution. After extracting the video frames of the gas–liquid reaction and the frames of background and compensation video, the image processing routine can be applied to each set of images to generate local concentration profiles of the three indigo carmine species. In the last step, these images of concentration profiles are compiled into a video. Three reaction videos are generated per operating point to ensure reproducibility.

### 3 | NUMERICAL METHODS

The high accuracy and computational efficiency of FeatFlow solver package relies on the employed state-of-art numerical methods. The basic solver is developed with Multilevel Pressure Schur Complement techniques to handle pressure–velocity coupling in Navier–Stokes equation. First, the time discretization is performed with one of conventional techniques (Crank–Nicolson for this study) while, the spatial discretization is carried out by higher-order finite elements with conforming isoparametric tri-quadratic (-linear) shape functions for velocities (concentrations) and piecewise-linear approximations for the pressures. The resulting linearized discrete systems of equations are solved with a geometric multigrid solver with problem adopted smoothers and grid transfer, which boosts the performance. Coarse grid problems are solved with distributed-memory parallel solvers.<sup>19</sup> The employed  $Q_2/P_1$  FE discretization is implicitly stable for laminar flow problems and requires no stabilization scheme, which suits well to simulate the flows in the scope of this study and leads to high accuracy by avoiding artificial corrections on the velocity field.<sup>20</sup> The employed numerical methods and techniques are discussed thoroughly in our previous study<sup>23</sup> and therein cited studies; in the following an overview of methods more specific to gas–liquid slug flow with chemical reaction is given.

An *interface tracking technique* (in an ALE approach) is implemented to accurately resolve the interface.<sup>23</sup> In our approach the mesh is deformed mostly due to the deformation of the interface, which is a result of the interplay between the hydrodynamic forces and the surface tension, as this interaction is visible in the governing Equations (1)–(3):

$$\rho(\mathbf{x}) \left[ \frac{\partial \mathbf{u}}{\partial t} + (\mathbf{u} \cdot \nabla) \mathbf{u} \right] - \nabla \cdot \boldsymbol{\sigma}(\mathbf{x}) = \rho(\mathbf{x}) \mathbf{f} + \mathbf{g}_\Gamma(\gamma); \quad \nabla \cdot \mathbf{u} = 0 \quad \text{in } \Omega(t) \quad (1)$$

$$[\boldsymbol{\sigma} \mathbf{n}] = \mathbf{g}_\Gamma(\Gamma, \mathbf{u}) = -\gamma \kappa \mathbf{n} \quad \text{on } \Gamma(t) \quad (2)$$

$$\mathbf{U}_\Gamma = (\mathbf{u} \cdot \mathbf{n}) \cdot \mathbf{n} \quad \text{on } \Gamma(t) \quad (3)$$

with  $\mathbf{x}$  as position vector,  $\mathbf{f}$  as body force,  $\boldsymbol{\sigma}$  as stress field,  $\mathbf{g}_\Gamma$  as surface tension force,  $\gamma$  as surface tension,  $\mathbf{n}$  as normal direction,  $\kappa$  as curvature of the interface,  $\mathbf{U}_\Gamma$  as velocity in normal direction to interface,  $\Omega$  as fluid domain and  $\Gamma$  as interface. The interfacial stress creates a

jump in the stress field ( $\boldsymbol{\sigma}(\mathbf{x}) = \nabla \cdot (l\mu + \mu(\mathbf{x}))[(\nabla \mathbf{u})^T + \nabla \mathbf{u}]$ ) at the sharp interface between two fluids domain  $\Omega_1$  and  $\Omega_2$  ( $\Omega = \Omega_1 \cup \Omega_2$ ); thus, we calculate RHS of Equation (2) by using *Laplace–Beltrami operator*. Employing higher-order *isoparametric*  $Q_2$  finite element to obtain the *discrete* counter part of the Laplace–Beltrami operator was the key to accurately calculate the interfacial force.<sup>23</sup>

In order to avoid the extreme mesh deformations due to the convection, we adopted a *moving reference frame*. Then, the deformation of the mesh occurs only due to the interface movement according to  $\mathbf{U}_\Gamma$ . Since interface points on the created aligned meshes are tracked, it is necessary to reformulate the problem in the ALE formulation.<sup>23</sup> The limited mesh deformation due to the surface tracking within the adopted ALE approach still deteriorates the mesh quality and leads to the loss-of-accuracy. Therefore, to realize the continuous-in-time ALE approach we needed to occasionally deform the mesh with a partial differential equation based grid-deformation technique, which requires the solution of minimization problem in terms of the deformation gradient  $\Delta\varphi$ :

$$\Delta\varphi(\mathbf{x}) := \nabla \cdot \left( (\nabla\varphi(\mathbf{x}))^T + \nabla\varphi(\mathbf{x}) \right) = 0 \quad \text{in } \Omega(t) \quad (4)$$

with well-defined boundary condition on  $\partial\Omega_0$ .

After obtaining the steady flow-field, we solved the coupled reaction-transport equation with an operator splitting approach; this allowed us to adopt different time-step sizes for the reaction and transport phenomena. The consecutive redox reactions (described in Krieger et al.<sup>24</sup>)

$$\begin{aligned} \frac{dc_{O_2}}{dt} &= -k_1 c_{O_2} c_{LIC} - k_2 c_{O_2} c_{Int} \\ \frac{dc_{LIC}}{dt} &= -k_1 c_{O_2} c_{LIC} & k_1 &= 6.349 \cdot 10^5 \text{ L mol}^{-1} \text{ s}^{-1} \\ \frac{dc_{Int}}{dt} &= k_1 c_{O_2} c_{LIC} - k_2 c_{O_2} c_{Int} & k_2 &= 22.409 \cdot 10^5 \text{ L mol}^{-1} \text{ s}^{-1} \\ \frac{dc_{KIC}}{dt} &= k_2 c_{O_2} c_{Int} \end{aligned} \quad (5)$$

are solved with a highly accurate numerical scheme which is based on the methods introduced by Shampine and Gordon.<sup>25</sup> The transport Equation (6) for the species is discretized by  $Q_1$  FE. A conservative and limited, accurate numerical scheme to solve the convection dominated problem is obtained by using algebraic flux correction<sup>26</sup> so that mass conservation is always guaranteed at the algebraic level, and the over- and under-shoots are avoided.

$$\frac{\partial c_i}{\partial t} + (\mathbf{u} \cdot \nabla) c_i - D_i \Delta c_i = h \quad \text{in } \Omega_1 \quad (6)$$

where  $h$  is the source/sink term and  $\Omega_1$  the liquid domain. Streamlines and numerical grid are depicted in Figure 4. The concentration of keto-indigo carmine after 6 s for a total flow rate of  $4 \text{ ml min}^{-1}$  and gas/liquid ratio of 0.33 is shown in the upper images; below a zoom into the numerical grid near the gas–liquid interface is given.

In order to compare the 3D results of the numerical simulations against experiments, we averaged the concentration field results. As integral information along the capillary's cross-section is obtained in the experiments, we have chosen 30 equidistant layers (rasters) for the numerical postprocessing and interpolated the concentration fields onto these rasters. Later, these interpolated 30 fields are averaged by weighting them with the corresponding volumes, so to obtain the final results to compare with the experiments, see Section 4.1.2.

## 4 | RESULTS AND DISCUSSION

### 4.1 | Fluid dynamics with mass transfer

Concentration profiles of the three indigo carmine species resulting from slug flow in a straight FEP tube are compared for dry slug flow and film slug flow. Figure 5 shows the concentration development at 2, 4, 6, 8, and 10 s for a total flow rate of  $4 \text{ ml min}^{-1}$  and a gas/liquid ratio of 0.5. Gas bubble and liquid slug length for film slug flow are both around twice as long as those of dry slug flow.

The concentration distribution depicts the typical behavior of slug flow.<sup>27</sup> Well mixed areas, such as near the interfaces, in the channel center and near the tube wall, are quickly oxidized. The well oxidized

area near the interfaces follows the shape of the bubbles; nonetheless, it is rather planar for dry slug flow and spherical for film slug flow. Mass transfer toward the stagnant areas, between core and wall (yellow leuco-indigo carmine containing areas in Figure 5), is dominated by diffusion and happens on a similar time scale for dry and film slug flow. The intermediate species occurs in the region where oxygen is transported via advection (interface, core, and wall area) and stagnant areas, where oxygen transport happens due to diffusion. Stagnant areas and areas containing intermediate product shrink over time due to diffusion of oxygen until leuco-indigo carmine is fully oxidized. Figure 4 supports this observation since oxygen containing streamlines close to the interface cannot reach these stagnant areas through advection.

Addition of polysorbate 80 results in coalescence of gas bubbles for gas/liquid flow ratios smaller than 1.0. Therefore, only the gas/liquid ratio of 1.0 was investigated for experiments with polysorbate 80, which leads to small liquid slugs and fast reaction progress. The concentration development over time for the three indigo carmine species is comparable to film slug flow without surfactant. Videos capturing the oxidation of leuco-indigo carmine for dry slug, film slug flow and film slug flow with surfactant (0.005% v/v) are provided in Supporting Information for a gas/liquid ratio of 1.0 at  $4 \text{ ml min}^{-1}$ .

**FIGURE 4** (top) streamlines and concentration development of keto-indigo carmine after 6 s for a total flow rate of  $4 \text{ ml min}^{-1}$  and gas/liquid ratio of 0.33; (bottom) zoom into numerical grid near the gas-liquid interface [Color figure can be viewed at [wileyonlinelibrary.com](http://wileyonlinelibrary.com)]

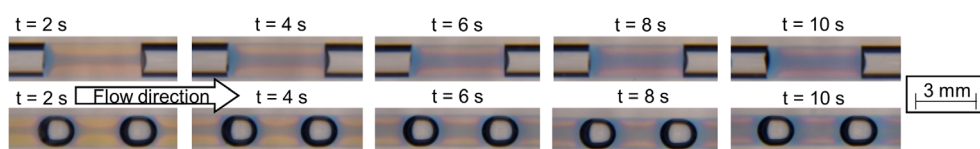
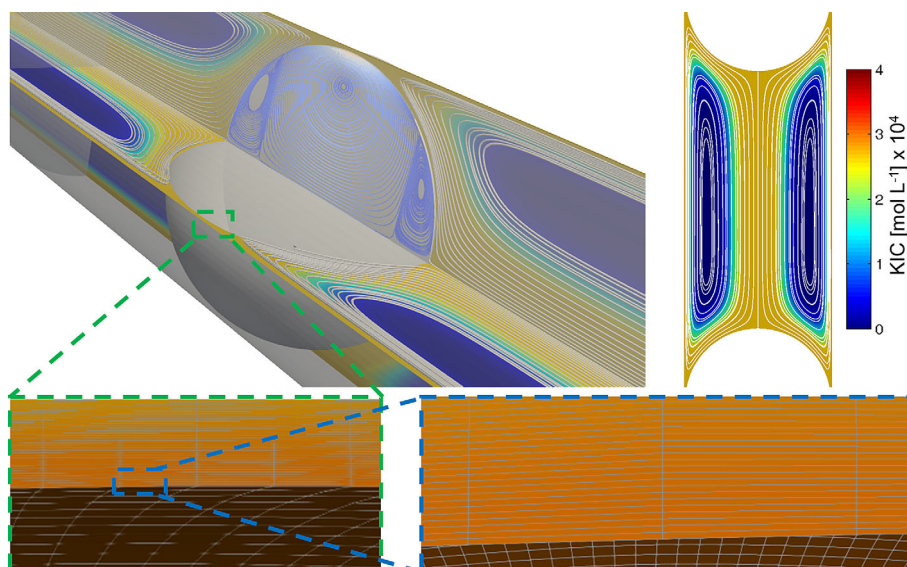


**FIGURE 5** Gas-liquid slug flow in FEP capillary with 1.6 mm inner diameter. Indigo carmine concentration development over 10 s in 2 s intervals for dry slug (top) and film slug (bottom) flow: Total flow rate =  $4 \text{ ml min}^{-1}$  and gas/liquid ratio = 0.5, but different slug length [Color figure can be viewed at [wileyonlinelibrary.com](http://wileyonlinelibrary.com)]

#### 4.1.1 | Effect of flow pulsation

During experiments in film slug flow, pulsation phenomena were observed, which did not occur in dry slug flow. Pressure loss for film slug flow (2,650–3,960 Pa m<sup>-1</sup>) is significantly lower than for dry slug flow (22,700–30,600 Pa m<sup>-1</sup>). Therefore, small pressure fluctuations during bubble formation are more impactful in film slug flow and are assumed to cause the pulsation. As a result, the flow velocity fluctuates as well and a jet stream caused by flow pulsation containing oxidized product travels through the center of the liquid slug widening the blue core stream. The described process happens periodically and is depicted in Figure 6. Dashed lines indicate the position of the pulse.

Effects of pulsation on mass transfer are discussed in Section 4.2. Further, this phenomenon is not considered in the numerical simulation and might lead to deviations between experimental and simulated data, which is described in the following sub-chapter.

#### 4.1.2 | Comparison with numerical simulation

Experimental data is generated by processing recorded videos as described in Sect. 2.3 and numerical results are obtained as described in Section 3. In Figure 7 experimental and simulated concentration profiles of the three different indigo carmine species are compared for

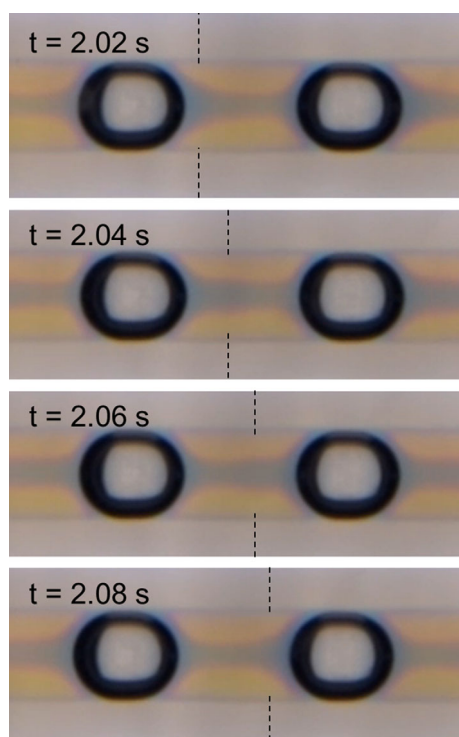


**FIGURE 6** Influence of pulsation on gas-liquid slug flow in FEP capillary with 1.6 mm inner diameter. Indigo carmine concentration development is shown in 20 ms intervals: Flow direction from left to right; total flow rate = 4 ml min<sup>-1</sup> and gas/liquid ratio = 0.5. Dashed lines indicate position of the thicker central jet as result of a pulse [Color figure can be viewed at [wileyonlinelibrary.com](http://wileyonlinelibrary.com)]

a volumetric flow rate of 4 ml min<sup>-1</sup> and gas/liquid ratios of 0.5 and 0.33 at the time steps  $t = 3$  and 6 s. A full comparison for the entire recorded time is given in Supporting Information for both cases. Note that the radical intermediate is depicted on a scale that is one order of magnitude smaller.

Both, the experimental and numerical results, describe the expected concentration profiles well, that is, keto-indigo carmine in the core stream, near the interface and the tube wall, and ring-shaped intermediate distribution in the transition zone between convection and diffusion dominated areas. The dynamics that can be seen in the experiments are captured precisely by the simulations at the different time steps. Particularly, the width of the core stream and the shape and thickness of the rings containing the intermediate product match well between simulation and experiment. It can be observed that the intermediate peak concentration shifts in radial direction toward the center of the stagnant zones. While this peak concentration is maintained during the experiments, it decreases in the simulations over time.

By integrating the concentration of the three indigo carmine species over the liquid volume and plotting these integrated quantities against time, a quantitative comparison is provided in Figure 8 for a total flow rate of 4 ml min<sup>-1</sup> and gas/liquid ratios of 0.5 (left) and 0.33 (right).

Over time leuco-indigo carmine is consumed due to the reaction and the fully oxidized product keto-indigo carmine is generated. Intermediate product remained at a low concentration level, approx. an order of magnitude smaller. The concentration profiles in the numerical simulations shows a faster consumption of leuco-indigo carmine and generation of keto-indigo carmine. During the image processing routine for the experimental data, areas near the bubble interface, which consist of mostly oxidized product, were masked and, therefore, could not be included in the integrated concentration values. This limitation partly causes the deviation between experimental and numerical results (Figures 7 and 8). Furthermore, the mass is not perfectly conserved in the experimental measurement and deviates by up to 23% from the average value, which was used for the numerical simulation. Despite these limitations a satisfactory match between experimental and simulated values is achieved for leuco-indigo carmine (average deviation = 28.9 and 21.3%, underpredicted) and keto-indigo carmine (average deviation = 57.6 and 57.1%, overpredicted) for a gas/liquid ratio of 0.5 and 0.33, respectively. The experimentally and numerically obtained concentration profiles of the intermediate product, which are much smaller than the other indigo-carmine species, do not agree well, there is a deviation of 85% for both cases. Average deviations are calculated as follows for each indigo carmine species:

$$g = \frac{1}{m} \sum_{i=1}^m \frac{\bar{c}_{i,\text{exp}} - \bar{c}_{i,\text{sim}}}{\bar{c}_{i,\text{exp}}} \quad (7)$$

with  $g$  as average deviation and  $\bar{c}_{i,\text{exp}}$  and  $\bar{c}_{i,\text{sim}}$  as averaged concentrations over liquid volume for experiments and numerical simulations, respectively. Low concentration levels of intermediate and occurrence in areas with limited oxygen availability result in comparably low

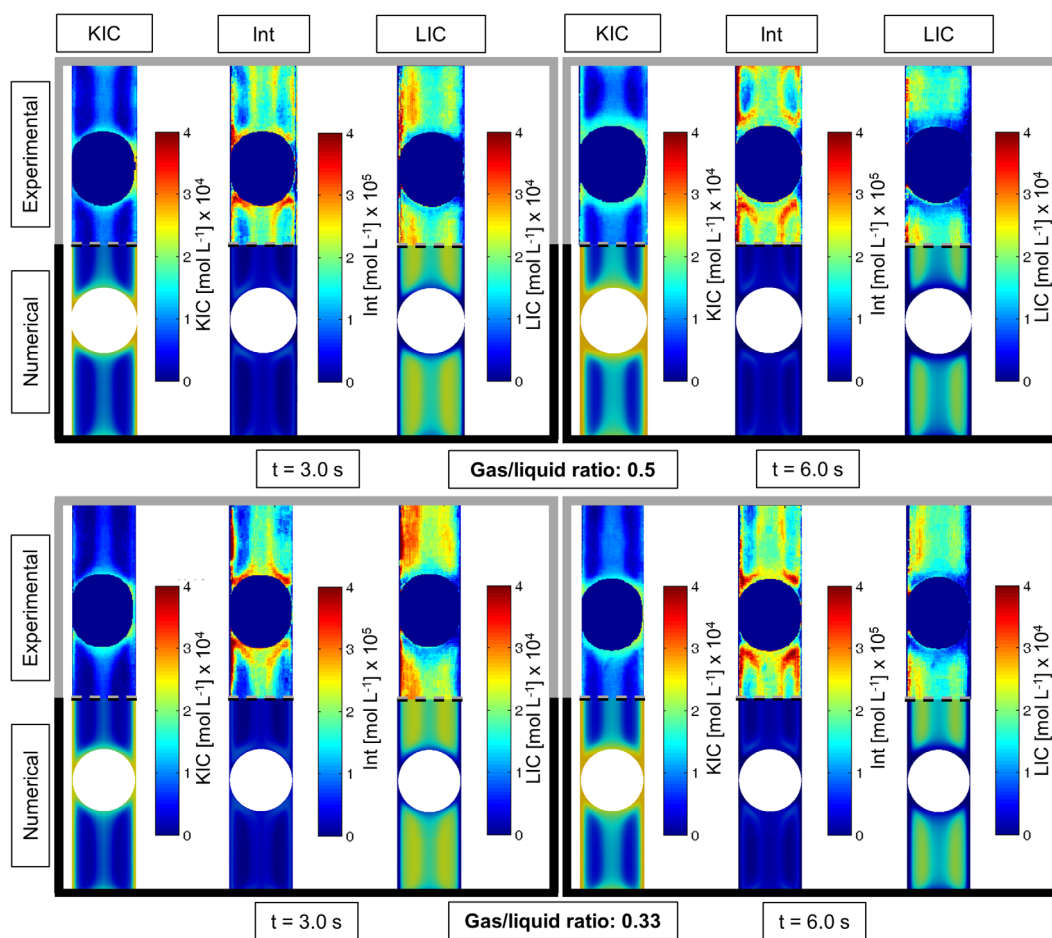
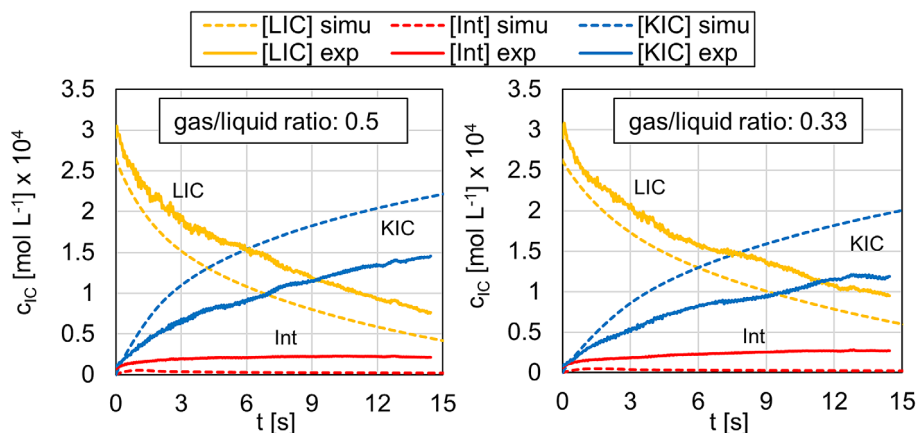


**FIGURE 7** Experimental and numerical concentration profiles of the three indigo carmine species: keto-indigo carmine (KIC), radical intermediate (Int), leuco-indigo carmine (LIC) at time steps  $t = 3.0$  and  $6.0$  s. Numerical concentration profiles are integrated over the cross-section. Total volumetric flow rate =  $4 \text{ ml min}^{-1}$ , gas/liquid ratios =  $0.5$  and  $0.33$ ,  $Re = 48$  [Color figure can be viewed at [wileyonlinelibrary.com](http://wileyonlinelibrary.com)]

**FIGURE 8** Integrated concentrations over slug volume for the three indigo carmine species plotted against time for a total volumetric flow rate of  $4 \text{ ml min}^{-1}$  and gas/liquid ratios of  $0.5$  (left) and  $0.33$  (right). Solid lines indicate experimental and dashed lines simulated results [Color figure can be viewed at [wileyonlinelibrary.com](http://wileyonlinelibrary.com)]



reaction rates and give more impact to advective and diffusive effects. Since the high concentration front of intermediate product is not resolved sufficiently accurate, the high concentration front smears out and partly causes this mismatch. We will resolve this problem in future work by employing a grid-adaptation technique based on the concentration gradient of oxygen; so that the regions of high

intermediate concentration will be dynamically resolved without excessive computational cost. The approach will be similar to the grid-adaptation technique near the interface, which is utilized in order to efficiently capture the hydrodynamics of gas-liquid slug flow. Another aspect is that the kinetic parameters used for the numerical simulations were determined assuming first-order kinetics regarding both

reactants.<sup>24</sup> By adjusting the kinetic parameters based on the numerical results, the match between experiments and simulations can be further improved (see Supporting Information).

## 4.2 | Mass transfer coefficients

From the local concentration profiles and the underlying stoichiometry<sup>9</sup> (Equation 8) the amount of absorbed oxygen can be calculated. Since dissolved oxygen cannot be measured with the current setup, this calculation is based on the assumption that the absorbed oxygen is fully converted to keto-indigo carmine and/or intermediate:

$$n_{O_2,cons} = n_{Int} + 2 \cdot n_{KIC} \quad (8)$$

with  $n_{O_2,cons}$ ,  $n_{IM}$ , and  $n_{KIC}$  as molar amount of consumed oxygen, intermediate and keto-indigo carmine, respectively. Enhancement of mass transfer due to the reaction has been found negligible in a previous study.<sup>24</sup> As a result, the amount of consumed oxygen is expected to follow a linear trend until saturation effects become relevant and oxygen accumulates in the liquid phase. The linear trend is described by following equation, which is derived in more detail in Dietrich et al.<sup>9</sup> and Krieger et al.<sup>11</sup>:

$$c_{O_2,cons} = \frac{k_L a \cdot c^* \cdot x_{tip}}{u_{TP}} \quad (9)$$

with  $k_L a$  as volumetric mass transfer coefficient,  $c^*$  as saturation concentration,  $x_{tip}$  as distance from needle tip, and  $u_{TP}$  as two-phase velocity. Consumed oxygen concentration  $c_{O_2,cons}$  describes a value that is equivalent to the amount of oxygen that was absorbed and consumed in the reaction according to Equation (8). Figure 9 shows an exemplary plot of  $c_{O_2,cons}$  against  $x_{tip}$  for a total flow rate of  $4 \text{ ml min}^{-1}$  and a gas/liquid ratio of 0.5 in film slug flow.

Indeed, a linear trend is observed near the needle tip before saturation effects and completed conversion near the interface result in a decline of the slope. The slope of the linear part is used to estimate

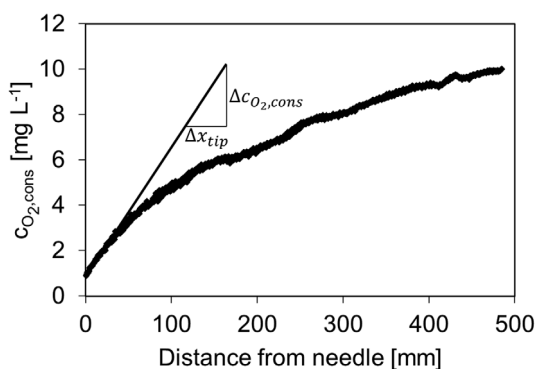


**FIGURE 9** Consumed oxygen concentration against distance from needle tip for total flow rate of  $4 \text{ ml min}^{-1}$  and gas/liquid ratio of 0.5 in film slug flow

mass transfer coefficients according to Equation (9). Some “bumps” in the graph are observable that are related to a tube that is not perfectly following a straight line. FEP is a stiff material and the tubes are transported in a coiled state. Even though a tension mechanism is applied in order to straighten the tube some minor deviations from the straight state persist and affect the image processing routine.

Volumetric mass transfer coefficients derived by the method described above are depicted in Figure 10 and measured in the range of  $0.160\text{--}0.554 \text{ s}^{-1}$  for film slug flow and  $0.099\text{--}0.420 \text{ s}^{-1}$  for dry slug flow, which is comparable to data from literature.<sup>28</sup>

At flow rates 8 and  $10 \text{ ml min}^{-1}$  for film slug flow smaller gas/liquid ratios than 1.0 could not be investigated, because the flow became unstable. Measured volumetric mass transfer coefficients are larger for film slug flow due to a higher specific surface area per liquid volume. For the same reason  $k_L a$  values increase with higher gas/liquid ratio at constant total flow rate, since higher gas/liquid ratios cause a decrease of liquid slug length and liquid volume. Regardless, slug and bubble lengths differ depending on whether film or dry slug flow is present and clear conclusions are difficult to draw.

To overcome this restriction, the specific interfacial area is estimated and used to calculate the  $k_L$  values. This approach allows for comparison of mass transfer for the different flow patterns by accounting for the varying slug lengths and the liquid film surrounding the gas bubbles in film slug flow. Interfacial area per liquid volume for dry slug flow is calculated by assuming a cylindrical shape for the bubble with two flat and circular interfaces, which leads to following expression:

$$a_{dry} = \frac{A_{Interface}}{V_L} = \frac{2}{L_{UC}(1-\epsilon_G)} \quad (10)$$

with specific interfacial area  $a$ , interfacial area per unit cell  $A_{Interface}$ , liquid volume per unit cell  $V_L$ , and unit cell length  $L_{UC}$ . A unit cell describes the repeating unit of slug flow consisting of gas bubble and liquid slug.<sup>12</sup>

For film slug flow a cylindrical part in the center of the gas bubble with two hemispherical caps is assumed. The cap diameter is approximated with the inner tube diameter  $d_i$ :

$$a_{film} = \frac{4 \cdot L_B}{d_i L_{UC}(1-\epsilon_G)} \quad (11)$$

with  $L_B$  as bubble length and  $\epsilon_G$  as gas hold up. Calculated  $k_L$  values are depicted in Figure 11 for film and dry slug flow at varying velocities and gas/liquid ratios.

With increasing flow rate, convective mixing increases leading to higher  $k_L$  values, which is seen in the experimental data. An increase of  $k_L$  values by 81% from  $4$  to  $10 \text{ ml min}^{-1}$  is observed for film slug flow and by 116% for dry slug flow. The operating point at  $6 \text{ ml min}^{-1}$  and a gas/liquid ratio of 0.33 for film slug flow is regarded as outlier. Issues with coalescence led to higher mass transfer in this case, which is also indicated by the larger error bars. Gas/liquid ratio on the other hand does not significantly affect the convective mixing within the



**FIGURE 10**  $k_L a$  values against total flow rate for film slug (left) and dry slug (right) flow at varying gas/liquid ratios. Flow became unstable for film slug flow at flow rates 8 and 10 mL min<sup>-1</sup> and gas/liquid ratios smaller than 1.0 and could not be evaluated

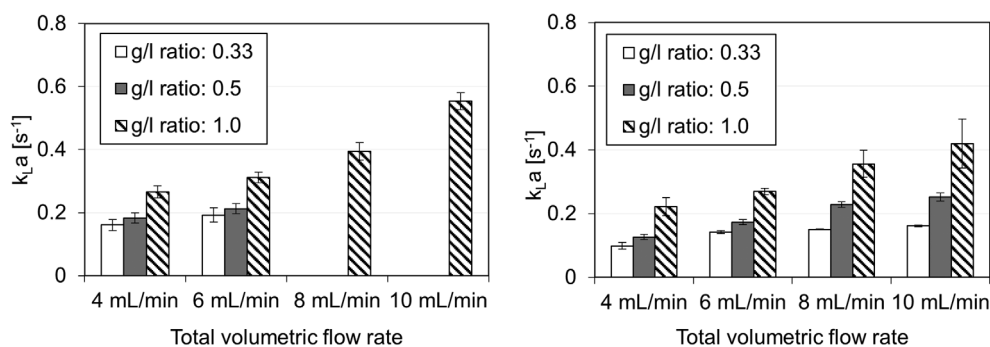
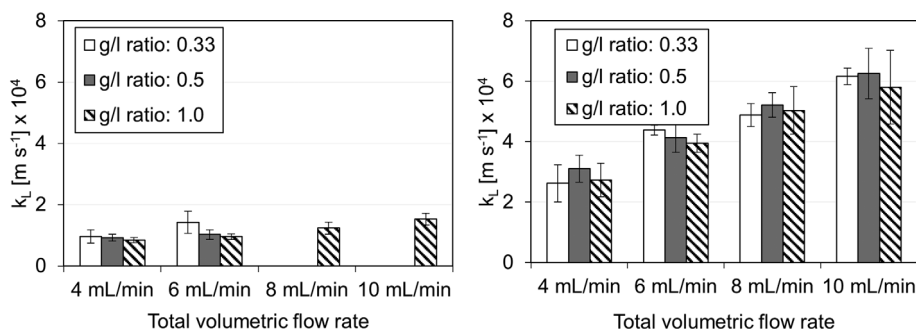


**FIGURE 11**  $k_L$  values against total flow rate for film (left) and dry (right) flow at varying gas/liquid ratios



liquid phase. Additionally, the bubble length remains constant at around 1.9 mm for film slug flow. Therefore, the contribution of the liquid film surrounding the bubbles does not change for different gas/liquid ratios and no significant effect of gas/liquid ratio on  $k_L$  values is observed.

Liquid-side mass transfer coefficients  $k_L$  for film slug flow are significantly lower compared to dry slug flow with less variation, which is indicated by the smaller error bars. Higher liquid-side mass transfer coefficients for dry slug flow can be related to stronger velocity gradients near the gas–liquid interface, which results in an intensified transfer of oxygen. Additionally, the flatter shape of the interface reduces the funneling effect caused by the Taylor vortices. Consequently, the core stream containing oxygen is wider for dry slug flow (Figure 5) and the convective distribution of oxygen is enhanced. Larger error bars for dry slug flow are caused by a stronger variation of slug and bubble lengths compared to film slug flow. Higher oxygen solubility due to increased pressure loss in dry slug flow was determined in preliminary experiments and is considered in the presented data. Note that the calculations for dry slug flow are based on the assumption of flat interfaces. In fact, the interfaces are slightly curved leading to an increased interfacial area. Therefore, the actual difference between  $k_L$  values for film and dry slug flow is smaller in reality.

#### 4.2.1 | Effect of surfactant

In order to study the effect of surfactant on mass transfer, concentration of polysorbate 80 was varied in the range of 0.005–0.1% v/v. In Figure 12  $k_L$  values for varying total flow rates and a set gas/liquid

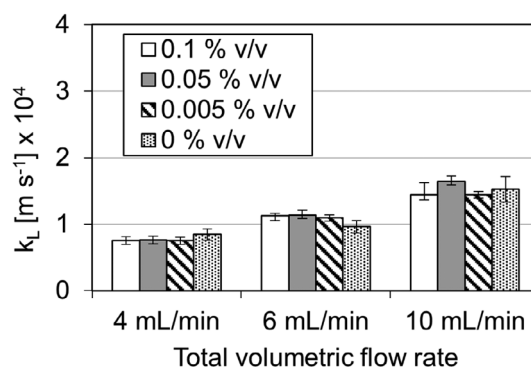


**FIGURE 12**  $k_L$  values against total flow rate for film slug flow and film slug flow with varying polysorbate 80 concentrations at gas/liquid ratio of 1.0

ratio of 1.0 are compared for film slug flow and film slug flow with surfactant.

Liquid-side mass transfer coefficients do not seem to be affected by the presence of surfactant at all, which is contradictory to literature.<sup>29–32</sup> Experiments in literature are commonly performed in columns with free rising bubbles, where decrease of mass transfer is observed when surfactant is present due to the stabilization of the gas–liquid interface, which provides less interfacial area for mass transfer. A transition in flow regime is observed from mobile surfaces to rigid spheres as the bubble shrinks.<sup>30</sup> Sardeing et al. reported that for a bubble size smaller than 1.5 mm this transition does not happen and only rigid spheres are observed leading to no significant difference between liquid-side mass transfer coefficients for “clean”

bubbles and bubbles containing surfactants.<sup>30</sup> In the present work, bubble sizes are in a similar order of magnitude ranging from 1.7 to 2.1 mm. Hence, the assumption is made that the observations for a free rising bubble can be transferred to bubbles in slug flow and that the shape of the bubble is additionally stabilized due to capillary forces leading to the shift toward higher bubble diameters, where surfactants do not influence mass transfer. As a result, polysorbate 80 can be used to generate film slug flow for the investigated reaction system in hydrophobic equipment, while allowing for transfer of conclusions to experiments without surfactants.

## 4.2.2 | Comparison with empirical and mathematical models

Measured mass transfer coefficients  $k_{L,a}$  are compared with correlations from literature. Correlations of Vandu et al.<sup>4</sup> and Yue et al.<sup>33</sup> are chosen for comparison since similar systems were studied, that is, air and water. Equations and operating conditions from those studies are summarized in Table 1 with  $D_{O_2}$  as diffusion coefficient of oxygen,  $u_B$  as bubble velocity and  $d_i$  as hydraulic diameter.  $D_{O_2} = 3.2 \cdot 10^{-9} \text{ m}^2 \text{ s}^{-1}$  has been measured by Yang et al.<sup>34</sup> for a similar solution containing the redox dye resazurin and is adopted for this work. Furthermore,  $k_{L,a}$  values are calculated according to van Baten's proposed model<sup>12</sup> and compared to the experimental data. The mathematical model is based on Higbie's penetration theory<sup>35</sup> and accounts for separated contributions of cap and film region:

$$k_{L,a} = k_{L,c}a_c + k_{L,f}a_f = \left( \frac{8 \cdot \sqrt{2}}{\pi \cdot L_{UC}} \sqrt{\frac{D_{O_2} u_B}{d_i}} + \frac{8(L_B - d_i)}{\sqrt{\pi} L_{UC} d_i} \sqrt{\frac{D_{O_2} u_B}{L_B - d_i}} \right) \cdot (1 - \varepsilon_G)^{-1} \quad (12)$$

where  $k_{L,c}a_c$  describes the contribution of the cap and  $k_{L,f}a_f$  the contribution of the film region. Equation (12) is based on a specific interfacial area that refers to the volume of the unit cell instead of liquid volume. Therefore, Equation (12) is adjusted by multiplication with the factor  $(1 - \varepsilon_G)^{-1}$  to match the experimental data. Note that the presented equations from literature are used to describe mass transfer in slug flow with a film surrounding the bubble. In order to describe

dry slug flow, Equation (12) is reduced to the contribution of the cap region and expressed with the  $k_L$  value and specific interfacial area for the dry slug flow geometry. Further, a factor  $F$  is included and fitted to the experimental data since the assumption of flat cylindrical interfaces might not be very accurate and a precise measurement is not possible with the presented setup. This factor should lie between 1.0 (flat cylindrical interface) and 1.6 (spherical interface):

$$k_{L,a} = k_{L,dry} a_{dry} = F \cdot \left( \frac{4}{\sqrt{\pi} \cdot L_{UC}} \sqrt{\frac{D_{O_2} u_B}{d_i}} \right) \cdot (1 - \varepsilon_G)^{-1} \quad (13)$$

Calculated and experimental volumetric mass transfer coefficients  $k_{L,a}$  are compared in Figure 13 for film and dry slug flow using the mathematical model by van Baten et al. (left) and for film slug flow using the correlations by Vandu et al. and Yue et al. (right). Values of 1 indicate a perfect match between calculated and experimental data.

The film slug flow model by van Baten et al. (Equation 12) overpredicts the volumetric mass transfer coefficients by a factor of 2.5–3.8. The experimental data is based on gas bubbles that are moving slowly and surrounded by a thin liquid film. Therefore, the influence of the liquid film is possibly overestimated in the mathematical model due to saturation of the liquid film. The saturation of the liquid film is described by the Fourier number  $Fo$ , which is defined as follows:

$$Fo = \frac{D_{O_2} t_{\text{Film}}}{\delta_{\text{Film}}^2} = \frac{D_{O_2} (L_B - d_i)}{\delta_{\text{Film}}^2 u_B} \quad (14)$$

with  $t_{\text{Film}}$  as contact time between liquid film and gas bubble and  $\delta_{\text{Film}}$  as film thickness, which is estimated by Bretherton's correlation.<sup>36</sup>

$$\delta_{\text{Film}} = 0.67 \cdot Ca^{2/3} d_i \quad (15)$$

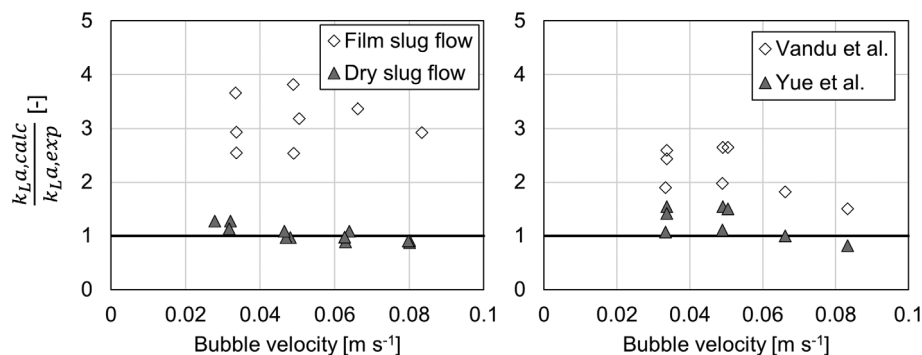
where  $Ca$  is the Capillary number. For  $Fo < 0.1$  it can be assumed that the film is not saturated.<sup>12</sup> The experiments in this work were performed for Fourier numbers ranging from 0.1 to 1.0, which indicates that saturation effects indeed could play an important role. This hypothesis is supported by the modified model (Equation 13) and the experimental data for dry slug flow. In this case, only the contribution of the cap region is considered resulting in a good match between calculated and experimental data. The fitted factor  $F$  is equal to 1.23, which suggests a reasonable interface shape that is between flat cylinders and spheres (coefficient of determination of 84%).

The correlation by Vandu et al. for film slug flow also overpredicts volumetric mass transfer coefficients by a factor of 1.5–2.6. In their work, Pyrex glass capillaries with longer unit cells, larger bubbles and higher velocities were investigated giving the liquid film more relevance. The correlation by Yue et al. is based on data with smaller unit cells in a PMMA channel (Table 1), which is closer to the experimental conditions in this work, despite the use of a rectangular channel. It describes this work's experimental data more accurately, especially for a gas/liquid ratio of 1.0. The deviation increases for lower gas/liquid

**TABLE 1** Correlations from literature to describe gas–liquid mass transfer in slug flow

Reference	Correlation	Conditions
4	$k_{L,a} = 4.5 \sqrt{\frac{D_{O_2} u_B}{L_{UC} d_i}}$	$d_i = 1.0; 2.0; 3.0 \text{ mm}$ (circular) $u_B = 0.09\text{--}0.65 \text{ m s}^{-1}$ $L_{UC} = 5\text{--}60 \text{ mm}$
33	$k_{L,a} = \frac{2}{d_h} \sqrt{\frac{D_{O_2} u_B}{d_h} \left( \frac{L_B}{L_{UC}} \right)^{0.3}}$	$d_h = 0.4 \text{ mm}$ (square) $u_B = 0.4\text{--}2.0 \text{ m s}^{-1}$ $L_{UC} = 0.96\text{--}3.8 \text{ mm}$
This work		$d_i = 1.6 \text{ mm}$ (circular) $u_B = 0.03\text{--}0.08 \text{ m s}^{-1}$ $L_{UC} = 3.0\text{--}10.5 \text{ mm}$

**FIGURE 13** Ratio of calculated and experimental  $k_L a$  values for varying flow rates: (left) model by van Baten et al. for film slug flow and adjusted equation for dry slug flow; (right) correlations of Vandu et al. and Yue et al. for film slug flow



ratios, that is, longer slugs and unit cells, which are outside of the investigated operating range of Yue et al.

Note that the experimental mass transfer coefficients increase stronger with higher velocities as the correlations and models suggest, which can be seen by the declining trend in both diagrams. This effect can be explained by the observed pulsation and the nonperfect straight capillary that affect the flow field stronger with increasing velocity.

## 5 | CONCLUSION AND OUTLOOK

A slider setup for bubble detection and tracking in slug flow was successfully constructed. The slider setup is based on open-source technology and is able to carry a DSLR camera for mass transfer analysis with high temporal and spatial resolution. Mass transfer was investigated for varying flow rates and gas/liquid ratios. Liquid-side mass transfer coefficients  $k_L$  were measured for dry slug flow in the range of  $2.6\text{--}6.3 \cdot 10^{-4} \text{ m s}^{-1}$  and for film slug flow in the range of  $0.8\text{--}1.5 \cdot 10^{-4} \text{ m s}^{-1}$ . For dry slug flow  $k_L$  values are assumed to be higher due to stronger velocity gradients near the interface. Polysorbate 80 was utilized to generate more stable film slug flow and its addition led to no measurable increase of mass transfer. Further, volumetric mass transfer coefficients  $k_L a$  were measured in the range of  $0.1\text{--}0.55 \text{ s}^{-1}$  for film and dry slug flow and compared with models and correlations from literature. Using these models and correlations film slug flow mass transfer could not be described precisely except for the correlation by Yue et al., which led to a good agreement for small unit cells. It appears that the contribution of the liquid film is significantly lower in this work, which is related to saturation effects in the film region due to low velocities and thin films. Furthermore, a model for dry slug flow based on the study by van Baten et al. is proposed (Equation 13) that predicts reasonable volumetric mass transfer coefficients, but requires further validation. This work highlights how open-source soft- and hardware can be implemented to enhance measurement techniques on a laboratory scale and abolish experimental restrictions. The experimental work is complemented with numerical simulations, where the complex process of combining advection, diffusion, and chemical reaction for slug flow was successful resulting in a fair match between experimental and numerical data for the reactant and fully oxidized product. After minor refinement of the numerical methods or adjustment of the kinetic parameters, it will be further

possible to describe the intermediate concentration with high accuracy.

In future work, the FeatFlow CFD software will be developed to tackle more complex setups such as helically coiled tubes and coiled flow inverters, where current analytical methods find some limitations. The fluid dynamics in this helical equipment will be numerically and experimentally studied in detail. Further, optimal operating conditions will be proposed in order to maximize (a) selectivity toward an intermediate product and (b) mass transfer for mass transfer limited reactions. Overall, the link between hydrodynamics, selectivity and mass transfer will be established to provide meaningful data and fundamental understanding for the scale-up of gas-liquid process and development of gas-liquid contactors.

## NOTATION

$a$	specific interfacial area per liquid volume ( $\text{m}^{-1}$ )
$A_{\text{interface}}$	interfacial area ( $\text{m}^2$ )
$c$	concentration ( $\text{mol m}^{-3}$ )
$c^*$	dissolved oxygen concentration at saturation ( $\text{mol m}^{-3}$ )
$c_{\text{O}_2, \text{cons}}$	consumed oxygen concentration ( $\text{mol m}^{-3}$ )
$D_i$	diffusion coefficient of species $i$ in alkaline glucose solution ( $\text{m}^2 \text{ s}^{-1}$ )
$d$	diameter (m)
$f$	body force ( $\text{m s}^{-2}$ )
$F$	fitting factor (–)
$g$	average deviation (–)
$g_{\Gamma}$	surface tension force ( $\text{kg m}^{-2} \text{ s}^{-2}$ )
$h$	source/sink term ( $\text{mol m}^{-3} \text{ s}^{-1}$ )
$k$	reaction rate coefficient ( $\text{L mol}^{-1} \text{ s}^{-1}$ )
$k_L$	liquid side mass transfer coefficient ( $\text{m s}^{-1}$ )
$k_L a$	volumetric mass transfer coefficient ( $\text{s}^{-1}$ )
$L$	length (m)
$n$	molar amount (mol)
$p$	pressure ( $\text{kg m}^{-1} \text{ s}^{-2}$ )
$u$	velocity ( $\text{m s}^{-1}$ )
$U_{\Gamma}$	velocity in normal direction of interface ( $\text{m s}^{-1}$ )
$t$	time (s)
$t_{\text{Film}}$	contact time with liquid film (s)
$\dot{V}$	volumetric flow rate ( $\text{m}^3 \text{ s}^{-1}$ )
$x_{\text{tip}}$	distance from needle tip to liquid slug ( $\text{m}^{-1}$ )

## Greek letters

$\gamma$	surface tension (kg s <sup>-2</sup> )
$\Gamma$	interface (–)
$\delta_{\text{Film}}$	liquid film thickness (m)
$\varepsilon$	void fraction/phase holdup (–)
$\mu$	dynamic viscosity (kg m <sup>-1</sup> s <sup>-1</sup> )
$\rho$	density (kg m <sup>-3</sup> )
$\sigma$	stress field (kg m <sup>-1</sup> s <sup>-2</sup> )
$\Omega$	domain (–)

## Dimensionless groups

Ca	Capillary number (=)	$\left(\frac{u\eta}{\gamma}\right)$
Fo	Fourier number (=)	$\left(\frac{D_{O_2} t_{\text{Film}}}{\delta_{\text{Film}}^2}\right)$
Re	Reynolds number (=)	$\left(\frac{\rho u d_i}{\eta}\right)$

## Subscripts

B	bubble
G	gas
h	hydraulic
i	inner
L	liquid
TP	two-phase
UC	unit cell

## Abbreviations

FEP	fluorinated ethylene propylene
IC	indigo carmine
Int	anionic radical intermediate
KIC	keto-indigo carmine
LIC	leuco-indigo carmine

## ORCID

Waldemar Krieger  <https://orcid.org/0000-0003-3914-0257>

## REFERENCES

- Kockmann N, Thenée P, Fleischer-Trebes C, Laudadio G, Noël T. Safety assessment in development and operation of modular continuous-flow processes. *React Chem Eng.* 2017;2(3):258-280.
- Plutschack MB, Pieber B, Gilmore K, Seeberger PH. The Hitchhiker's guide to flow chemistry. *Chem Rev.* 2017;117(18):11796-11893.
- Kockmann N. *Transport phenomena in micro process engineering.* Berlin: Springer; 2008.
- Vandu CO, Liu H, Krishna R. Mass transfer from Taylor bubbles rising in single capillaries. *Chem Eng Sci.* 2005;60(22):6430-6437.
- Kurt SK, Warnebold F, Nigam KDP, Kockmann N. Gas-liquid reaction and mass transfer in microstructured coiled flow inverter. *Chem Eng Sci.* 2017;169:164-178.
- Yao C, Dong Z, Zhao Y, Chen G. An online method to measure mass transfer of slug flow in a microchannel. *Chem Eng Sci.* 2014;112:15-24.
- Kuhn S, Jensen KF. A pH-sensitive laser-induced fluorescence technique to monitor mass transfer in multiphase flows in microfluidic devices. *Ind Eng Chem Res.* 2012;51(26):8999-9006.
- Butler C, Cid E, Billet A-M. Modelling of mass transfer in Taylor flow: investigation with the PLIF-I technique. *Chem Eng Res des.* 2016;115:292-302.
- Dietrich N, Loubière K, Jimenez M, Hébrard G, Gourdon C. A new direct technique for visualizing and measuring gas-liquid mass transfer around bubbles moving in a straight millimetric square channel. *Chem Eng Sci.* 2013;100:172-182.
- Kováts P, Pohl D, Thévenin D, Zähringer K. Optical determination of oxygen mass transfer in a helically-coiled pipe compared to a straight horizontal tube. *Chem Eng Sci.* 2018;190:273-285.
- Krieger W, Lamsfuß J, Zhang W, Kockmann N. Local mass transfer phenomena and chemical selectivity of gas-liquid reactions in capillaries. *Chem Eng Technol.* 2017;40(11):2134-2143.
- van Baten JM, Krishna R. CFD simulations of mass transfer from Taylor bubbles rising in circular capillaries. *Chem Eng Sci.* 2004;59(12):2535-2545.
- Falconi CJ, Lehrenfeld C, Marschall H, et al. Numerical and experimental analysis of local flow phenomena in laminar Taylor flow in a square mini-channel. *Phys Fluids.* 2016;28(1):12109.
- Fitzpatrick DE, Battilocchio C, Ley SV. Enabling technologies for the future of chemical synthesis. *ACS Cent Sci.* 2016;2(3):131-138.
- O'Brien M, Cooper DA, Dolan J. Continuous flow iodination using an automated computer-vision controlled liquid-liquid extraction system. *Tetrahedron Lett.* 2017;58(9):829-834.
- O'Brien M, Konings L, Martin M, Heap J. Harnessing open-source technology for low-cost automation in synthesis: flow chemical deprotection of silyl ethers using a homemade autosampling system. *Tetrahedron Lett.* 2017;58(25):2409-2413.
- Gutierrez JMP, Hinkley T, Taylor JW, Yanev K, Cronin L. Evolution of oil droplets in a chemorobotic platform. *Nat Commun.* 2014;5:5571.
- Kockmann N, Bittorf L, Krieger W, Reichmann F, Schmalenberg M, Soboll S. Smart equipment—a perspective paper. *Chemie Ingenieur Technik.* 2018;90(11):1806-1822.
- Razzaq M, Damanik H, Hron J, Ouazzi A, Turek S. FEM multigrid techniques for fluid-structure interaction with application to hemodynamics. *Appl Numer Math.* 2012;62(9):1156-1170.
- Bayraktar E, Mierka O, Turek S. Benchmark computations of 3D laminar flow around a cylinder with CFX. *OpenFOAM and FeatFlow IJCE.* 2012;7(3):253.
- Sousa MM, Miguel C, Rodrigues I, et al. A photochemical study on the blue dye indigo: from solution to ancient Andean textiles. *Photochem Photobiol Sci.* 2008;7(11):1353-1359.
- Mizutani Y, Tomiyama A, Hosokawa S, Sou A, Kudo Y, Mishima K. Two-phase flow patterns in a four by four rod bundle. *J Nucl Sci and Technol.* 2007;44(6):894-901.
- Turek S, Mierka O, Bäuml K. Numerical benchmarking for 3D multiphase flow: new results for a rising bubble. In: Radu F, Kumar K, Berre I, Nordbotten J, Pop I, eds. *Numerical Mathematics and Advanced Applications. Lecture Notes in Computational Science and Engineering.* Vol 126. Berlin: Springer; 2019:593-601.
- Krieger W, Hörbelt M, Schuster S, Hennekes J, Kockmann N. Kinetic study of leuco-indigo carmine oxidation and investigation of Taylor and Dean flow superposition in a coiled flow inverter. *Chem Eng Technol.* 2019;42(10):2052-2060.
- Shampine LF, Gordon MK. *Computer solution of ordinary differential equations: the initial value problem.* San Francisco: Freeman; 1975.
- Kuzmin D. Algebraic flux correction for finite element approximation of transport equations. Numerical mathematics and advanced applications. Proceedings of ENUMATH 2005, The 6th European conference on numerical mathematics and advanced applications, Santiago de Compostela, Spain; 2006; Berlin: Springer. pp. 345-353.
- Dittmar I, Ehrhard P. Numerische Untersuchung einer Flüssig/flüssig-Pfropfenströmung in einem Mikrokapillarreaktor. *Chemie Ingenieur Technik.* 2013;85(10):1612-1618.

28. Wang K, Luo G. Microflow extraction: a review of recent development. *Chem Eng Sci.* 2017;169:18-33.
29. Painmanakul P, Loubière K, Hébrard G, Mietton-Peuchot M, Roustan M. Effect of surfactants on liquid-side mass transfer coefficients. *Chem Eng Sci.* 2005;60(22):6480-6491.
30. Sardeing R, Painmanakul P, Hébrard G. Effect of surfactants on liquid-side mass transfer coefficients in gas-liquid systems: a first step to modeling. *Chem Eng Sci.* 2006;61(19):6249-6260.
31. Vasconcelos JMT, Rodrigues JML, Orvalho SCP, Alves SS, Mendes RL, Reis A. Effect of contaminants on mass transfer coefficients in bubble column and airlift contactors. *Chem Eng Sci.* 2003;58(8):1431-1440.
32. Vasconcelos JMT, Orvalho SP, Alves SS. Gas-liquid mass transfer to single bubbles: effect of surface contamination. *AIChE J.* 2002;48(6):1145-1154.
33. Yue J, Luo L, Gonthier Y, Chen G, Yuan Q. An experimental study of air-water Taylor flow and mass transfer inside square microchannels. *Chem Eng Sci.* 2009;64(16):3697-3708.
34. Yang L, Dietrich N, Hébrard G, Loubière K, Gourdon C. Optical methods to investigate the enhancement factor of an oxygen-sensitive colorimetric reaction using microreactors. *AIChE J.* 2016;63(6):2272-2284.
35. Higbie R. The rate of absorption of a pure gas into a still liquid during short periods of exposure. *Trans AIChE.* 1935;31:365-389.
36. Bretherton FP. The motion of long bubbles in tubes. *J Fluid Mech.* 1961;10(2):166-188.

#### SUPPORTING INFORMATION

Additional supporting information may be found online in the Supporting Information section at the end of this article.

**How to cite this article:** Krieger W, Bayraktar E, Mierka O, et al. Arduino-based slider setup for gas-liquid mass transfer investigations: Experiments and CFD simulations. *AIChE J.* 2020;66:e16953. <https://doi.org/10.1002/aic.16953>